

Optimal ridge orientation estimator using integrated second directional derivative

Desikachari Nadadur

Siemens Medical Solutions USA, Inc.
Ultrasound Group
Image Processing, Applications Solutions Group
Box 7002, Issaquah, Washington 98029-7002
E-mail: dnadadur@comcast.net

Robert M. Haralick

The City University of New York
Graduate Center
New York, New York 10016

David E. Gustafson

Siemens Medical Solutions USA, Inc.
Ultrasound Group
Box 7002, Issaquah, Washington 98029-7002

Abstract. *In this paper, we discuss a unified theory for and performance evaluation of the ridge direction estimation through the minimization of the integral of the second directional derivative of the gray-level intensity function. The primary emphasis of this paper is on the ridge orientation estimation. The subsequent ridge detection can be performed using the traditional methods of using the zero crossing of the first directional derivative. The performance evaluation of the ridge orientation estimation is performed in terms of the mean orientation bias and orientation standard deviation given the true orientation and the same two measures given the noise standard deviation. We discuss two forms of our new ridge detector—first (ISDDRO-CN) using the noise covariance matrix estimation procedure under colored noise assumption, and the second (ISDDRO-WN) using the white noise assumption. ISDDRO-CN performs better than the ISDDRO-WN in the presence of strong correlated noise. When the noise levels are moderate it performs as well as ISDDRO-WN. ISDDRO-CN has superior noise sensitivity characteristics. We also compare both forms of our algorithm with the algorithm, Maximum Level Set Extrinsic Curvature (MLSEC) designed by A. López [IEEE Trans. Patter Anal. Mach. Intell. 21, 327–335 (1999)]. © 2005 SPIE and IS&T. [DOI: 10.1117/1.1901683]*

1 Introduction

Ridges in digital images occur when gray-level intensities of a simply connected sequence of pixels are significantly higher than those of the neighboring sequences. The extent of disparity of brightness levels between the sequences will depend on the distribution of brightness values surrounding the sequence, and the length of the sequence. Intuitively, the *ridge line* can be understood as the path traced, when we walk along the top of a mountain range with valleys on both our left and right sides. The ridge line can have several

forms—the ridge line can slope downward, upward or be flat when you walk along it, still maintaining the valleys on both sides. The case in which a ridge is flat is called *flat ridge*. Therefore, if you walk across the ridge (i.e., orthogonal to the ridge line), we first go uphill, reach the peak and then go downhill on the other side. The profile of an *ideal step ridge* is shown in Fig. 1(a) and that of an *ideal ramp ridge* is shown in Fig. 1(b). A more realistic ridge is the one shown in Fig. 2 and also shown are corresponding first and second derivatives.

Some of the prominent papers on ridge detection in general imaging are in Refs. 1–10. Also, proposed were several ridge operators for more general applications such as *multiscale image analysis*,^{11–14} *image topographic classification*,^{15–22} recently, more attention has been paid to the application of ridge feature extractors to *terrain feature identification*,^{23–25} *shape-from-shading*,²⁶ *digital portal imaging*²⁷ (a type of clinical x-ray imaging), in *unimodality*,²⁸ and *multimodality medical image registration*,^{29,30} *fingerprint identification*^{31–34} and *enhancement*,^{13,35} *medial line transformation*,³⁶ *skeletonization*,³⁷ and *medical image segmentation*.^{38,39}

In this paper, we discuss a unified theory for and performance evaluation of the ridge direction estimation through the minimization of the integral of the second directional derivative of the gray-level intensity function. The performance evaluation of the ridge direction operator is performed as a function of the perturbation on the gray-level intensity function of the input digital image. We are mainly interested in the optimal estimation of the ridge orientation.

We use the fact that along the ridge profile the first derivative has a zero-crossing where the ridge attains its peak value and has a negative second derivative at the same

Paper 03085 received Jun. 9, 2003; revised manuscript received May 31, 2004; accepted for publication Nov. 29, 2004; published online May 12, 2005.
1017-9909/2005/\$22.00 © 2005 SPIE and IS&T.

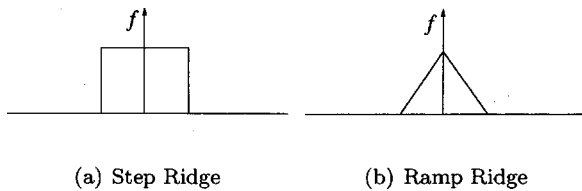


Fig. 1 Illustration of an ideal ridge profiles.

location (Fig. 2). Therefore, once we find the *optimal* direction along which the second directional derivative has the smallest value (i.e., largest negative value), we can then find the zero-crossing of the first directional derivative along that estimated direction. If the zero-crossing is sufficiently close to the center of the pixel and the second directional derivative has sufficient magnitude, we can then label the pixel as the ridge pixel.⁴⁰

For simplicity, we call this the *Integrated Second Directional Derivative Ridge Operator* (ISDDRO) in the rest of this paper. The bias and the variance of the ridge direction estimate are the objective measures of performance. We use a bivariate fourth order polynomial function as our facet model of the image intensity function in the neighborhood of a given size. We assume a *zero mean Gaussian* perturbation model for the observed image intensity function. We develop the ridge operator under two different noise models: (1) white noise and (2) colored noise. In the latter case, we use the procedure described in Refs. 41 and 42 to estimate the noise covariance matrix, and use the corresponding expression for the estimation of the facet model coefficients. We compare the performance of our ridge operator in terms of the optimal ridge direction estimation under both the covariance models and also against the operator Maximum Level Set Extrinsic Curvature (MLSEC), developed by López *et al.*²² They do not perform the performance evaluation of their algorithm the way we intend to do here. We perform the performance evaluation of the ridge direction estimate with respect to the direction estimate bias and direction estimate standard deviation. We use these two parameters while comparing with the MLSEC operator. MLSEC operator works on the same principles of looking for the negative second directional derivative at the zero-crossing of the first directional derivatives. However,

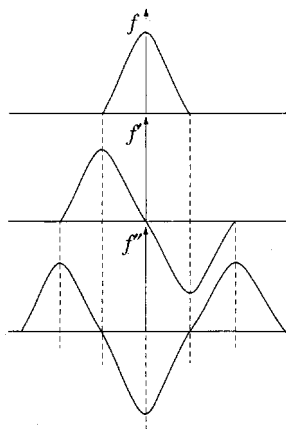


Fig. 2 Illustration of a more realistic ridge profile.

the derivatives and then the divergence are obtained by using the centered differences in the smallest neighborhood (3×3), and then searching for the zero-crossings to label the ridge pixels. The images are first regularized using a Gaussian kernel. The orientation of the second derivatives are computed by using their components in x and y directions in the same smallest neighborhood, as,

$$\theta_{mlsec} = \arctan\left(\frac{y}{x}\right). \tag{1}$$

Here we use the simple version of the operator as opposed to the one using the structure tensor (MLSEC-ST) by the same authors.

Our procedure for Ridge detection from gray-level images involves the following steps:

1. Noise covariance matrix estimation as described in Refs. 41 and 42.
2. Estimating the underlying gray-level surface in the neighborhood of the pixel under consideration using a Bayesian approach.
3. Estimating the optimal direction θ that minimizes the integral of the second directional derivative of the fitted facet model of the gray-level intensity surface.
4. Given this optimal direction, if the negatively sloped zero crossing of the first directional derivative occurs in the neighborhood of the center pixel, and the second directional derivative is negative and has sufficient magnitude, then we label it as a ridge pixel. However, in this paper we do not focus on the ridge labeling.

1.1 Organization of the Paper

In Sec. 2, we describe the facet model and the noise model that we use. Section 3 discusses the estimation of the facet model parameters under colored and white noise assumptions. In Sec. 4, we derive the optimal ridge orientation estimate. Section 5 discusses the procedure for labeling a pixel as a ridge pixel. We discuss the performance evaluation of the ridge direction estimate in Sec. 6. Finally, in Sec. 7, we summarize the results of this paper.

2 The Facet Model and the Noise Model

2.1 The Facet Model

For the n th image neighborhood, we can write the facet model⁴⁰ representing the ideal noise free signal energy as,

$$s_n = \mathbf{B} \alpha_n, \tag{2}$$

where s_n represent the $n=1, \dots, N$; $K=(2R+1) \times (2R+1)$ -dimensional noiseless vectors from the signal space, where R is the half-width of the discrete support of the neighborhood; \mathbf{B} is an *orthonormal* matrix whose columns represent the *Discrete Orthonormal Polynomial* (DOP) basis of the space modeled to contain the signal energy, and α_n are $n=1, \dots, N$; M -dimensional vectors of coefficients (also known as *DOP coefficients*) of the facet model. \mathbf{B} is obtained as discussed in Refs. 40, 41, and 43.

In the rest of the paper, we will use the terms, *DOP coefficients* and *facet model coefficients* interchangeably.

2.2 The Noise Model

Let x_n ; $n=1, \dots, N$ be the NK -dimensional independent samples of the noisy observed signal. Then, the facet model represents this noisy signal as^{41,42}

$$x_n = B\alpha_n + \eta_n, \tag{3}$$

where $\eta_n \sim \mathcal{N}(\mathbf{0}, \Sigma_\eta)$ are the independent identically distributed Gaussian random variates. In general, Σ_η represents the covariance matrix of a colored noise signal. Under the white noise assumption, $\Sigma_\eta = \sigma^2 \mathbf{I}$, where σ^2 is the variance of the white noise.

3 Estimation of the Facet Model Coefficients

We reproduce the results here from Refs. 41 and 42 for convenience of explanation. Under the colored noise assumption the DOP coefficients, used for fitting to the image gray level data, for the n th neighborhood are given by,

$$\hat{\alpha}_n = (B' - \Sigma_{BC} \Sigma_{CC}^{-1} C') x_n, \tag{4}$$

where C is an *orthonormal* matrix whose columns span the space (noise space) that is *orthogonal complement* to the space (signal space) spanned by the columns of B , Σ_{CC} is Σ_η expressed in the orthogonal complement space and Σ_{BC} depicts the extent of correlation between the two spaces. The noise covariance matrix is estimated as discussed in the said references.

Under white noise assumption, these coefficients are written,

$$\hat{\alpha}_n = B' x_n. \tag{5}$$

Therefore, in the following sections, when we mention that the ridge operator uses colored noise assumption, we mean that it uses the DOP coefficients given by Eq. (4), and when we say the ridge operator uses the white noise assumption, then we mean that it uses the DOP coefficients given by Eq. (5).

4 The Ridge Operator

For ridge detection, we use a *bivariate fourth order polynomial* as our facet model describing the gray-level intensity surface in a local neighborhood. This is because of the higher order ridge behavior compared to an edge. Further, if any order less than 4 (say, a cubic) is used, then it will produce an undesirable result of the ridge direction estimate becoming independent of the integration domain size.

Let $J(r, c)$ denote the gray-level of the image J at (r, c) in the *row-column* coordinate system. We know that the DOP basis is defined over a discrete support or region of a given size. For this reason, we will have different basis matrix B for different sized supports. Therefore, to make our functional form of the gray-level surface independent of the support size, we will express it, for a given (r, c) , in *canonical form* as,

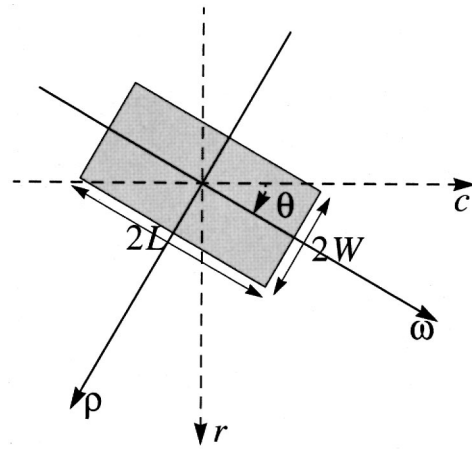


Fig. 3 Illustration of the integrated second directional derivative ridge operator.

$$f(r, c) = k_1 + k_2 r + k_3 c + k_4 r^2 + k_5 r c + k_6 c^2 + k_7 r^3 + k_8 r^2 c + k_9 r c^2 + k_{10} c^3 + k_{11} r^4 + k_{12} r^3 c + k_{13} r^2 c^2 + k_{14} r c^3 + k_{15} c^4, \tag{6}$$

where, *canonical coefficients* $k = (k_1, k_2, \dots, k_{15})'$ is the vector of DOP coefficients α expressed in canonical form. This is the *bivariate fourth order polynomial* model for the noise-free underlying gray-level intensity function.

The DOP coefficients α_n of the facet model are related to the corresponding canonical coefficients k_n through the relation,

$$k_n = T_{\alpha \rightarrow k} \alpha_n, \tag{7}$$

where the transformation matrix $T_{\alpha \rightarrow k}$ is described in Ref. 10. Using DOP bases instead of the canonical basis allows us to estimate the DOP coefficients α_n , independently of one another which can easily be converted to canonical form.

Therefore, we can express the uncertainty in the canonical coefficients k_n as,

$$\Sigma_{\hat{k}} = T_{\alpha \rightarrow k} \Sigma_{\hat{\alpha}} T'_{\alpha \rightarrow k}. \tag{8}$$

Estimating the optimal ridge direction: We estimate the optimal ridge direction by finding the minimum of the integral of the second directional derivative of $f(r, c)$, taken over all possible directions. Such an approach proved to provide least bias and variance⁴⁴ of the estimated direction in the case of edge detection.

Let

$$r = \rho \cos \theta + \omega \sin \theta; \quad c = -\rho \sin \theta + \omega \cos \theta. \tag{9}$$

This is the polar representation of the lines and ρ and ω are the axes along the length and the width of the domain of integration used in determining the ridge direction, as shown in Fig. 3. $\theta \in [0, 2\pi)$ is the angle of orientation, measured clockwise with respect to the column axis and represents the direction forming the rectangular domain of integration of length $2L$ and width $2W$ centered at the origin of

the coordinate system, and is orthogonal to the lines along which the integrated second directional derivative is measured. The second directional derivative of $f(r, c)$ along a line in the direction θ (using polar form of lines) is given by

$$f_{\theta\theta}(r, c) = \frac{\partial^2 f}{\partial r^2} \sin^2 \theta + 2 \frac{\partial^2 f}{\partial r \partial c} \sin \theta \cos \theta + \frac{\partial^2 f}{\partial c^2} \cos^2 \theta, \quad (10)$$

where $(\cdot)_{\theta\theta}$ denotes the second directional derivative.

Using Eq. (6), we obtain the following results:

$$\frac{\partial^2 f(r, c)}{\partial r^2} = 2k_4 + 6k_7 r + 2k_8 c + 12k_{11} r^2 + 6k_{12} r c + 2k_{13} c^2, \quad (11)$$

$$\frac{\partial^2 f(r, c)}{\partial c^2} = 2k_6 + 2k_9 r + 6k_{10} c + 2k_{13} r^2 + 6k_{14} r c + 12k_{15} c^2, \quad (12)$$

$$\frac{\partial^2 f(r, c)}{\partial r \partial c} = k_5 + 2k_8 r + 2k_9 c + 3k_{12} r^2 + 4k_{13} r c + 3k_{14} c^2. \quad (13)$$

Substituting for r and c from Eq. (9) into the above equation, and simplifying,

$$\begin{aligned} \frac{\partial^2 f}{\partial r^2} = & (12k_{11} \cos^2 \theta - 6k_{12} \sin \theta \cos \theta + 2k_{13} \sin^2 \theta) \rho^2 \\ & + (24k_{11} \sin \theta \cos \theta + 6k_{12}(\cos^2 \theta - \sin^2 \theta) \\ & - 4k_{13} \sin \theta \cos \theta) \rho \omega + (12k_{11} \sin^2 \theta \\ & + 6k_{12} \sin \theta \cos \theta + 2k_{13} \cos^2 \theta) \omega^2 + (6k_7 \cos \theta \\ & - 2k_8 \sin \theta) \rho + (6k_7 \sin \theta + 2k_8 \cos \theta) \omega + 2k_4, \quad (14) \end{aligned}$$

$$\begin{aligned} \frac{\partial^2 f}{\partial c^2} = & (2k_{13} \cos^2 \theta - 6k_{14} \sin \theta \cos \theta + 12k_{15} \sin^2 \theta) \rho^2 \\ & + (4k_{13} \sin \theta \cos \theta + 6k_{14}(\cos^2 \theta - \sin^2 \theta) \\ & - 24k_{15} \sin \theta \cos \theta) \rho \omega + (2k_{13} \sin^2 \theta \\ & + 6k_{14} \sin \theta \cos \theta + 12k_{15} \cos^2 \theta) \omega^2 + (2k_9 \cos \theta \\ & - 6k_{10} \sin \theta) \rho + (2k_9 \sin \theta + 6k_{10} \cos \theta) \omega + 2k_6, \quad (15) \end{aligned}$$

$$\begin{aligned} \frac{\partial^2 f}{\partial r \partial c} = & (3k_{12} \cos^2 \theta - 4k_{13} \sin \theta \cos \theta + 3k_{14} \sin^2 \theta) \rho^2 \\ & + (6k_{12} \sin \theta \cos \theta + 4k_{13}(\cos^2 \theta - \sin^2 \theta) \\ & - 6k_{14} \sin \theta \cos \theta) \rho \omega + (3k_{12} \sin^2 \theta \\ & + 4k_{13} \sin \theta \cos \theta + 3k_{14} \cos^2 \theta) \omega^2 + (2k_8 \cos \theta \\ & - 2k_9 \sin \theta) \rho + (2k_8 \sin \theta + 2k_9 \cos \theta) \omega + k_5. \quad (16) \end{aligned}$$

Substituting the above expressions into Eq. (10) and simplifying, we get,

$$f_{\theta\theta}(\rho \cos \theta + \omega \sin \theta, -\rho \sin \theta + \omega \cos \theta) = A\rho^2 + B\rho\omega + C\omega^2 + D\rho + E\omega + F, \quad (17)$$

where

$$\begin{aligned} A = & 2k_{13} \sin^4 \theta + 6(k_{14} - k_{12}) \sin^3 \theta \cos \theta + (12k_{11} - 8k_{13} \\ & + 12k_{15}) \sin^2 \theta \cos^2 \theta + 6(k_{12} - k_{14}) \sin \theta \cos^3 \theta \\ & + 2k_{13} \cos^4 \theta, \quad (18) \end{aligned}$$

$$\begin{aligned} B = & -6k_{12} \sin^4 \theta + 12(2k_{11} - k_{13}) \sin^3 \theta \cos \theta \\ & + 18(k_{12} - k_{14}) \sin^2 \theta \cos^2 \theta \\ & + 12(k_{13} - 2k_{15}) \sin \theta \cos^3 \theta + 6k_{14} \cos^4 \theta, \quad (19) \end{aligned}$$

$$\begin{aligned} C = & 12k_{11} \sin^4 \theta + 12k_{12} \sin^3 \theta \cos \theta + 12k_{13} \sin^2 \theta \cos^2 \theta \\ & + 12k_{14} \sin \theta \cos^3 \theta + 12k_{15} \cos^4 \theta, \quad (20) \end{aligned}$$

$$\begin{aligned} D = & -2k_8 \sin^3 \theta + 2(3k_7 - 2k_9) \sin^2 \theta \cos \theta \\ & + 2(2k_8 - 3k_{10}) \sin \theta \cos^2 \theta + 2k_9 \cos^3 \theta, \quad (21) \end{aligned}$$

$$\begin{aligned} E = & 6k_7 \sin^3 \theta + 6k_8 \sin^2 \theta \cos \theta + 6k_9 \sin \theta \cos^2 \theta \\ & + 6k_{10} \cos^3 \theta, \quad (22) \end{aligned}$$

$$F = 2k_4 \sin^2 \theta + 2k_5 \sin \theta \cos \theta + 2k_6 \cos^2 \theta. \quad (23)$$

Now, define,

$$\begin{aligned} \mathcal{F}_{\theta\theta} = & \frac{1}{4LW} \int_{-W}^W \int_{-L}^L f_{\theta\theta}(\rho \cos \theta + \omega \sin \theta, -\rho \sin \theta \\ & + \omega \cos \theta) d\rho d\omega, \quad (24) \end{aligned}$$

where L and W are the half-length and half-width, respectively, of the domain of integration.

Evaluating the above integral using Eq. (17), we get,

$$\mathcal{F}_{\theta\theta} = \frac{1}{3}(AL^2 + BW^2 + 3F), \quad (25)$$

where A , B , and F are as defined earlier.

Most of the applications use square neighborhoods, for ease of computation. Therefore, we let $L = W$ for the rest of the discussion.

Theorem 1 (Optimal ridge direction): Using ISDDRO, the optimal direction estimate $\hat{\theta}$ of θ is given by,

$$\hat{\theta} = \frac{1}{2} \arctan\left(\frac{D_1}{D_2}\right), \quad (26)$$

where

$$D_1 = L^2(k_{12} + k_{14}) + k_5, \quad (27)$$

$$D_2 = 2L^2(k_{15} - k_{11}) + k_6 - k_4. \quad (28)$$

Proof: The result is obtained by finding $\hat{\theta}$ that minimizes $\mathcal{F}_{\theta\theta}$. By substituting the values of A , B , and F into Eq. (25), we get

$$\begin{aligned} \mathcal{F}_{\theta\theta} = & \frac{1}{3}[2(L^2k_{13} + 6W^2k_{11})\sin^4\theta + 6((k_{14} - k_{12})L^2 \\ & + 2k_{12}W^2)\sin^3\theta\cos\theta + 4((3k_{11} - 2k_{13} + 3k_{15})L^2 \\ & + 3k_{13}W^2)\sin^2\theta\cos^2\theta + 6((k_{12} - k_{14})L^2 \\ & + 2k_{14}W^2)\sin\theta\cos^3\theta + 2(k_{13}L^2 + 6k_{15}W^2)\cos^4\theta \\ & + 6k_4\sin^2\theta + 6k_5\sin\theta\cos\theta + 6k_6\cos^2\theta]. \end{aligned} \quad (29)$$

For square neighborhoods, letting $L = W$, we have

$$\begin{aligned} \mathcal{F}_{\theta\theta} = & \frac{1}{3}[2L^2(k_{13} + 6k_{11})\sin^4\theta + 6L^2(k_{14} + k_{12})\sin^3\theta\cos\theta \\ & + 4L^2(3k_{11} + k_{13} + 3k_{15})\sin^2\theta\cos^2\theta + 6L^2(k_{12} \\ & + k_{14})\sin\theta\cos^3\theta + 2L^2(k_{13} + 6k_{15})\cos^4\theta \\ & + 6k_4\sin^2\theta + 6k_5\sin\theta\cos\theta + 6k_6\cos^2\theta]. \end{aligned} \quad (30)$$

To compute an estimate $\hat{\theta}$ of θ that minimizes $\mathcal{F}_{\theta\theta}$, we differentiate $\mathcal{F}_{\theta\theta}$ with respect to θ , equate it to zero and solve the resulting equation for θ ,

$$\begin{aligned} \frac{\partial \mathcal{F}_{\theta\theta}}{\partial \theta} = & \frac{1}{3}[8L^2(k_{13} + 6k_{11})\sin^3\theta\cos\theta + 6L^2(k_{14} + k_{12}) \\ & \times (-\sin^4\theta + 3\sin^2\theta\cos^2\theta) + 4L^2(3k_{11} + k_{13} \\ & + 3k_{15})(-2\sin^3\theta + 2\sin\theta\cos^3\theta) \\ & + 6L^2(k_{12} + k_{14})(-3\sin^2\theta\cos^2\theta + \cos^4\theta) \\ & - 8L^2(k_{13} + 6k_{15})\cos^3\theta\sin\theta + 12k_{14}\sin\theta\cos\theta \\ & + 6k_5(-\sin^2\theta + \cos^2\theta) - 12k_6\cos\theta\sin\theta]. \end{aligned} \quad (31)$$

Simplifying the above equation, we get,

$$\begin{aligned} \frac{\partial \mathcal{F}_{\theta\theta}}{\partial \theta} = & \frac{1}{3}[(6L^2(k_{12} + k_{14}) + 6k_5)\cos 2\theta + (12L^2(k_{11} - k_{15}) \\ & + 6(k_4 - k_6))\sin 2\theta]. \end{aligned} \quad (32)$$

Equating the above to zero, and solving for θ , we get the estimate $\hat{\theta}$ as,

$$\hat{\theta} = \frac{1}{2} \arctan\left(\frac{L^2(k_{12} + k_{14}) + k_5}{2L^2(k_{15} - k_{11}) + k_6 - k_4}\right). \quad (33)$$

□

Once we find the optimal estimate $\hat{\theta}$ of θ as given in Eq. (26), we then apply Haralick's conditions, discussed in Sec. 5.1, to label the center pixel as a ridge pixel. The direction orthogonal to $\hat{\theta}$ is the ridge direction. In the next section we describe an algorithm to label a given pixel as a ridge pixel.

5 Labeling of Ridges

In this section, we describe an algorithm one can use to label the center pixel of fitting neighborhood as a ridge pixel, after the *optimal* ridge orientation has been estimated.

5.1 Haralick's Condition for Ridge Pixel Classification

We use Haralick's condition⁴⁰ in determining if a given pixel is a ridge pixel. This condition is stated as follows: A ridge occurs where there is a local maximum in one direction. Therefore, it must have a negative second directional derivative in the direction across the ridge and also a zero first directional derivative in the same direction. The direction in which the local maximum occurs may correspond to either of the directions in which the curvature is *extremized*, since the ridge itself may be curved. Therefore, we have the following cases and a pixel is classified as a ridge pixel, if it satisfies any of these cases:

1. Nonflat ridge.

$$\|\nabla f\| \neq 0, \quad \lambda_1 < 0, \quad \nabla f \cdot \omega_1 = 0. \quad (34)$$

2. Flat ridge. In this case, the ridge line is horizontal, and the gradient along it is zero. The defining characteristic is that the second directional derivative in the direction of the ridge line is zero and that the second directional derivative across the ridge line is negative.

$$\|\nabla f\| = 0, \quad \lambda_1 < 0, \quad \lambda_2 = 0, \quad (35)$$

where

- ∇f = gradient vector of a function f ,
- $\|\nabla f\|$ = gradient magnitude,
- ω_1 = unit vector in the direction in which the second directional derivative has the greatest magnitude,
- ω_2 = unit vector orthogonal to ω_1 ,
- λ_1 = value of the second directional derivative in the direction ω_1 ,
- λ_2 = value of the second directional derivative in the direction ω_2 ,
- $\nabla f \cdot \omega_1$ = value of the first directional derivative in the direction of ω_1 ,
- $\nabla f \cdot \omega_2$ = value of the first directional derivative in the direction of ω_2 .

Without loss of generality we assume that $|\lambda_1| \geq |\lambda_2|$.

Geometrically, the condition $\nabla f \cdot \omega_1 = 0$ means that the gradient direction, which is defined for nonzero gradients, is orthogonal to the direction ω_1 of extremized curvature.

5.2 Ridge Pixel Classification

As we know an extremum occurs at a point where the first derivative has a zero crossing. Once we have the estimate $\hat{\theta}$ of θ that extremizes the second directional derivative of the polynomial function describing the gray level surface, we

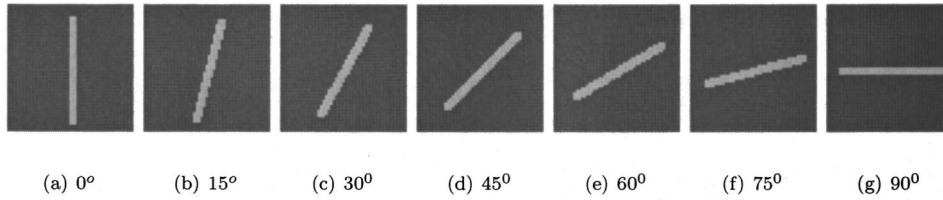


Fig. 4 Noise-free step ridge images.

find the zero crossing of its first directional derivative along $\hat{\theta}^\perp$, that is closest to the center of the pixel at the center of the neighborhood. Then, we apply the Haralick's conditions to determine whether to label the pixel as *ridge* or not. Remember that $\hat{\theta}$ is, in fact, orthogonal to the direction in which the integrated second directional derivative is extremized.

Therefore, we search in the direction $\hat{\theta}^\perp$ and restrict (r, c) as,

$$r = \omega \sin \hat{\theta}^\perp, \quad c = \omega \cos \hat{\theta}^\perp. \quad (36)$$

Now, the bivariate fourth order discrete orthogonal polynomial function can be written as

$$f(\omega; \hat{\theta}^\perp) = S\omega^4 + T\omega^3 + U\omega^2 + V\omega + W, \quad (37)$$

where

$$S = k_{11} \sin^4 \hat{\theta}^\perp + k_{12} \sin^3 \hat{\theta}^\perp \cos \hat{\theta}^\perp + k_{13} \sin^2 \hat{\theta}^\perp \cos^2 \hat{\theta}^\perp + k_{14} \sin \hat{\theta}^\perp \cos^3 \hat{\theta}^\perp + k_{15} \cos^4 \hat{\theta}^\perp, \quad (38)$$

$$T = k_7 \sin^3 \hat{\theta}^\perp + k_8 \sin^2 \hat{\theta}^\perp \cos \hat{\theta}^\perp + k_9 \sin \hat{\theta}^\perp \cos^2 \hat{\theta}^\perp + k_{10} \cos^3 \hat{\theta}^\perp, \quad (39)$$

$$U = k_4 \sin^2 \hat{\theta}^\perp + k_5 \sin \hat{\theta}^\perp \cos \hat{\theta}^\perp + k_6 \cos^2 \hat{\theta}^\perp,$$

$$V = k_2 \sin \hat{\theta}^\perp + k_3 \cos \hat{\theta}^\perp, \quad (40)$$

$$W = k_1.$$

The first directional derivative is given by

$$f_\omega(\omega; \hat{\theta}^\perp) = 4S\omega^3 + 3T\omega^2 + 2U\omega + V. \quad (41)$$

This is a cubic polynomial in the free variable ω and we solve for it by equating this expression to zero. The cubic has either three real roots or has one real root and two

complex conjugate roots. In the case where we get complex conjugate roots, we discard them and consider only the real root, because we are working in real space. By normalizing the equation, by dividing it by $4S$ which is the coefficient of ω^3 , the cubic can be written as

$$\omega^3 + T_1\omega^2 + U_1\omega + V_1 = 0, \quad (42)$$

where $T_1 = 3T/4S$, $U_1 = U/2S$, and $V_1 = V/4S$. This equation is easily solved by using procedures described in Ref. 45. Let $\hat{\omega}_1$ be the real root with the least magnitude. We say that $\hat{\omega}_1$ is the closest to the center of the pixel, if $|\hat{\omega}_1| \leq \text{distance threshold}$ where an extremum of interest is found. If Haralick's conditions given in Sec. 5.1 and $|f_{\omega\omega}(\omega; \hat{\theta}^\perp)| > \text{curvature threshold}$ are satisfied we label center pixel to be a *ridge* pixel.

6 Performance Evaluation of Ridge Direction Estimation

As mentioned earlier, we use the *bias* and *variance* of the estimated ridge direction to measure the performance of the ridge direction estimation.

Let ψ_θ be the *bias* in the estimated ridge direction and is given by

$$\psi_\theta = (\bar{\theta} - \tilde{\theta}), \quad (43)$$

where $\tilde{\theta}$ is the *true* direction and the sample mean, $\bar{\theta}$ is given by,

$$\bar{\theta} = \frac{1}{N} \sum_{i=1}^N \hat{\theta}_i \quad (44)$$

and N is the number of estimates $\hat{\theta}$ which are obtained as discussed in the next section.

Let σ_θ^2 be the *variance* of the ridge direction estimate and is given by,

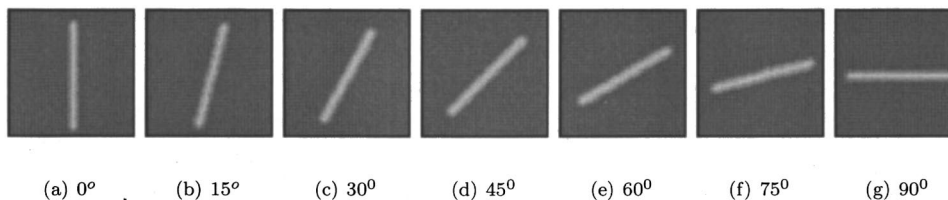


Fig. 5 Noise-free ramp ridge images.

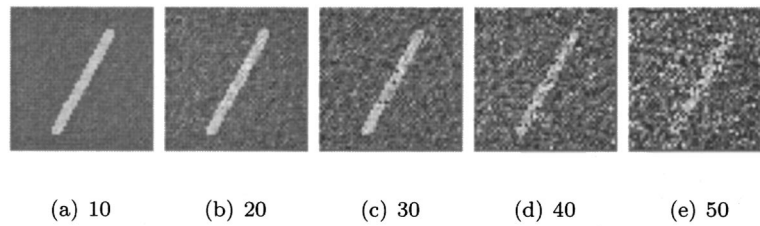


Fig. 6 Noisy step ridge images oriented at 30°, for different values of noise standard deviation σ_η .

$$\sigma_\theta^2 = \frac{1}{N-1} \sum_{i=1}^N (\hat{\theta}_i - \bar{\theta})^2. \quad (45)$$

In the following analysis, we denote the *integrated second directional derivative ridge operator* (ISDDRO) operator using *white noise* by ISDDRO-WN and that using the *colored noise* by ISDDRO-CN.

6.1 Synthetic Image Generation

Performance evaluation is performed on the image data generated by placing a ridge in a known direction and adding randomly generated *colored* noise, with a given standard deviation and a correlation matrix, to the pixels in the image. We assume a ridge contrast of 100 for the noise-free images, i.e. we use a value of 200 for the ridge pixels and 100 for nonridge pixels. We varied the orientation θ^\perp across the ridge, from 0° to 90°. Images of size 51 rows and 51 columns were generated [Image generation method: (1) an ideal surface is defined, (2) a sampling grid is placed on the ideal surface, (3) the sampled value is then quantized. There is a relationship between the coordinate systems of the ideal surface and the sampling grid. In reality the sampling grid is not applied to the surface with the two coordinate systems aligned. This can be achieved by adding a random displacement $D \in [-\frac{1}{2}, \frac{1}{2}]$ to the center pixel of the image through which the ridge is assumed to pass.] to contain two types of ridges: (1) step ridges; (2) ramp ridges. Step ridges are generated by creating a digital line in the given orientation and then performing a binary dilation to produce a 3-pixel wide line. Note that when a continuous line is digitized an orientation error occurs⁴⁶ and this error is dependent on the length of the line and its orientation. Since the lines that we use are smaller in length, this error becomes more pronounced. An angle of 30° in continuous domain may not be 30° in digital domain with the same Euclidean length. This is one of the reasons why we get large differences in the mean orientation bias and orienta-

tion standard deviation computed for two adjacent angles. However, this effect can be safely ignored while comparing different ridge operators as it is presented to all of them.

Ramp ridges are created by averaging the step ridges by a 3×3 averaging filter. We, then, added *colored* noise to these images by choosing a *correlation matrix*, \mathbf{Y}_η and by varying the standard deviation, σ_η , from 0 to 50. Covariance matrix Σ_η is given by $\sigma_\eta^2 \mathbf{Y}_\eta$. Mean value was set to zero. For each combination of θ^\perp and σ_η (given the \mathbf{Y}_η) we generated 1200 images with different noise instantiations. The ridge operator is applied to all the images using a 5×5 neighborhood centered at the center pixel of the images.

Note that, in the simulation experiments performed below, at orientations closer to 90° the sense of direction of the estimated orientation may get reversed due to the presence of large amounts of noise. For example, 87° may get estimated to be closer to -90°. In that case, performing an average of the directions may result in a value that is close to zero, producing a bias that is close to 90°. This type of behavior is acceptable for orientations from 0° up to and including 45°, but not for other orientations. Therefore, we follow the convention that whenever the estimated direction is less than or equal to -45°, we consider its absolute value in the sample mean computation, otherwise we use it without modification. This is done only for these simulated experiments. However, in real imagery when ridge detection is being considered this is not necessary.

Figures 4 and 5 show noise-free step and ramp ridge images, respectively, at some representative orientations. Examples of noisy versions of step and ramp images for an orientation of 30° for different values of the noise standard deviation are given in Figs. 6 and 7. Because we are using colored noise to contaminate the noise-free images, the perturbation is very strong. By the time we reach $\sigma_\eta = 50$, the images become very noisy and the structures of interest almost become indistinguishable from the perturbation.

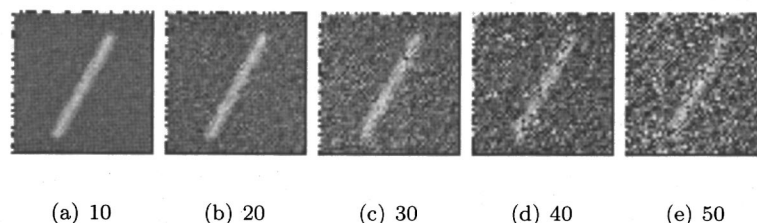


Fig. 7 Noisy ramp ridge images oriented at 30°, for different values of noise standard deviation σ_η .

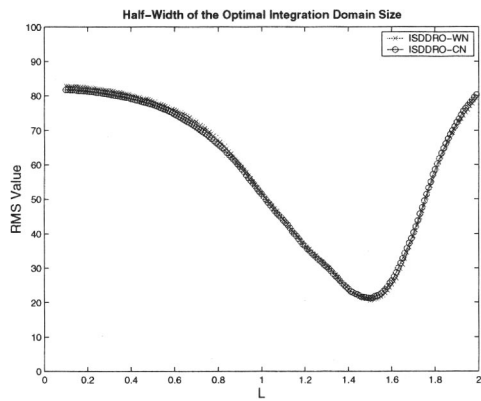


Fig. 8 Determination of the half-width L of the domain of integration for both step and ramp ridges under colored as well as white noise assumptions.

6.2 Optimal Integration Domain Size

Optimal integration domain size, $2L$, is obtained by applying the ridge operator to the center pixel of all the step and ramp images generated above and over all the orientations, using a 5×5 neighborhood. We combined the two performance measures, *orientation bias mean* and *orientation standard deviation* in a root-mean-squared (RMS) sense, i.e., the square root of the sum of squared orientation bias mean and orientation variance. Optimal integration domain size was determined for both the cases of colored noise and white noise assumption. In the former, the noise covariance matrix is estimated for each standard deviation-correlation matrix combination using a subset of images (to create approximately, 10 000 vectors). The value of L that produces the least RMS value is the optimal integration domain size. In our experiments, we found that a half-width of the integration domain size, L , of 1.5 was optimal for both step and ramp ridges in colored as well as white noise cases for a 5×5 neighborhood size. At the optimal L , the RMS value was 21.25 in the colored noise case and 20.635 in the white noise case. Plots given in Fig. 8 are the numerical results for the optimal integration domain size determination.

6.3 Performance Evaluation

In this section, we discuss the performance evaluation and comparison of ISDDRO-WN, ISDDRO-CN, and MLSEC operators. Recall, that the test images were created by adding colored noise with a given noise standard deviation, σ_η and correlation matrix, \mathbf{Y}_η . When applying ISDDRO-CN operator, we estimate the noise covariance matrix as discussed in the previous sections and perform the evaluation using it. For ISDDRO-WN operator we estimate the variance of the noise under white noise assumption. We performed the experiments using a 5×5 neighborhood size. MLSEC operator requires that a Gaussian smoothing of the image with a specified scale be performed. We use a scale of 0.5 which results in a neighborhood size of 5×5 . Here we show the plots for the case when $\sigma_\eta = 20$.

6.3.1 True orientation versus mean orientation bias

For each combination of σ_η and \mathbf{Y}_η , each of the operators are applied to the center of the test images for given true orientation and several estimates for that orientation are obtained. We then compute the mean bias and plot them. We perform this for both the step ridge and ramp ridge images. Figures 9(a) and 9(b) show the plots for step and ramp ridge images. For step ridges, ISDDRO-CN has a worst case absolute bias of 15.891° , ISDDRO-WN has a worst case absolute bias of 14.965° , and MLSEC has a worst case absolute bias of 39.718° . For ramp ridges, ISDDRO-CN has a worst case absolute bias of 8.355° , ISDDRO-WN has a worst case absolute bias of 8.415° and MLSEC has a worst case absolute bias 23.742° . For step ridges, from the graph it is clear that ISDDRO-CN performance better than ISDDRO-WN in some cases and performs worse in other cases when step ridges are used. Over all angles, with respect to this measure, we can say that ISDDRO-CN performs slightly better than ISDDRO-WN for step ridges. As is evident both operators outperform MLSEC significantly. For ramp ridges, ISDDRO-CN performs better than ISDDRO-WN in most cases, and both operators outperform the MLSEC operator.

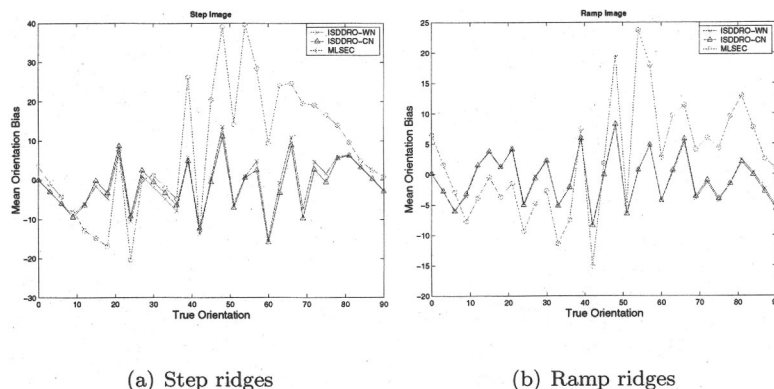


Fig. 9 Mean orientation bias plotted against the true orientation. The noise standard deviation is set to 20.

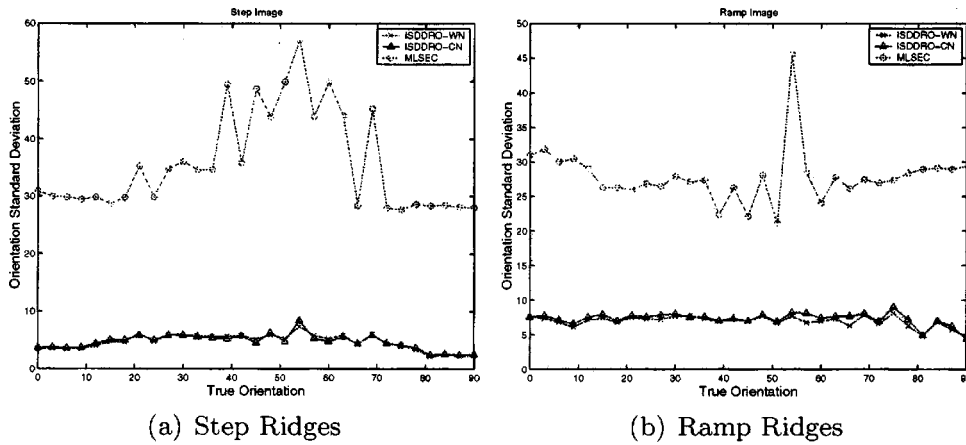


Fig. 10 Orientation standard deviation plotted against the true orientation. The noise standard deviation is set to 20.

6.3.2 True orientation versus orientation standard deviation

For each combination of σ_η and Y_η , each of the operators are applied to the center of the test images for given true orientation and several estimates for that orientation are obtained. We then compute the standard deviations of the orientation estimate by taking the square-root of the computed sample variance and plot them. We perform this for both the step ridge and ramp ridge images. Figures 10(a) and 10(b) show the plots for step and ramp ridge images. For step ridges, ISDDRO-CN operator produces the worst case orientation standard deviation of 8.42° when the true orientation is 54° and for ramp ridges it produces 9.012° at a true orientation of 75° . ISDDRO-WN produces the worst case orientation standard deviation of 7.375° at a true orientation angle of 54° , for step ridges. For ramp ridges it produces 8.115° at a true orientation of 75° . MLSEC operator produces a worst case standard deviation of 57.126° at a true orientation of 54° for the step ridges and produces 45.494° at a true orientation of 54° for ramp ridges. Over all angles, with respect to this measure, we can say that ISDDRO-CN performs better than ISDDRO-WN for step ridges. However, for ramp ridges ISDDRO-WN performs

slightly better than the ISDDRO-CN operator. As it is evident both operators out-perform MLSEC significantly.

6.3.3 Noise standard deviation versus mean orientation bias

For this and the next test we fix a true orientation and the noise correlation matrix, Y_η and vary the noise standard deviation, σ_η . For each standard deviation we compute the mean orientation bias and orientation standard deviation for the given true orientation. We perform this for both step and ramp ridge images. Figures 11(a) and 11(b) show the mean orientation bias plotted against the noise standard deviation for step and ramp ridges, respectively. For these plots, we held the true orientation at 30° . For step ridges, ISDDRO-CN produces mean bias close to zero and performs better than the ISDDRO-WN. MLSEC has the poorest noise sensitivity as the mean bias monotonically increases with σ_η , for step ridges. ISDDRO-CN and ISDDRO-WN follow each other very closely up until $\sigma_\eta = 30$ after which ISDDRO-CN performs better than ISDDRO-WN as σ_η approaches 50. MLSEC, again displays a poor noise sensitivity. It proves that under this per-

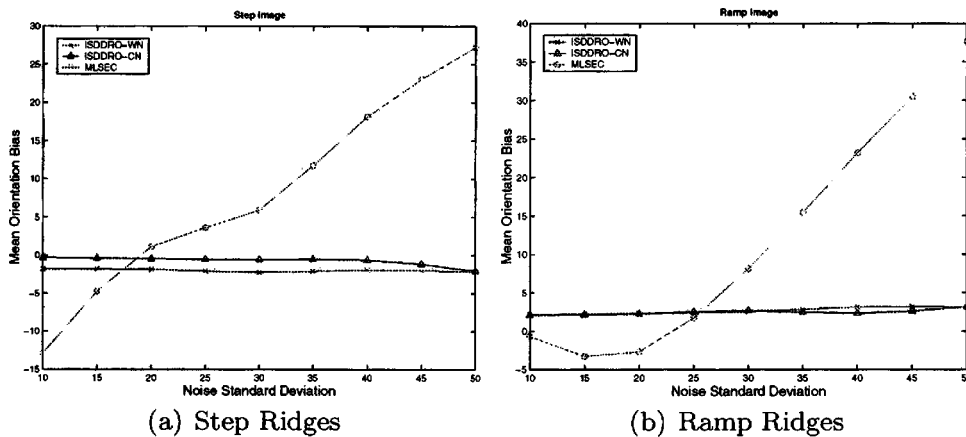


Fig. 11 Mean orientation bias plotted against the noise standard deviation. The orientation set to 30° .

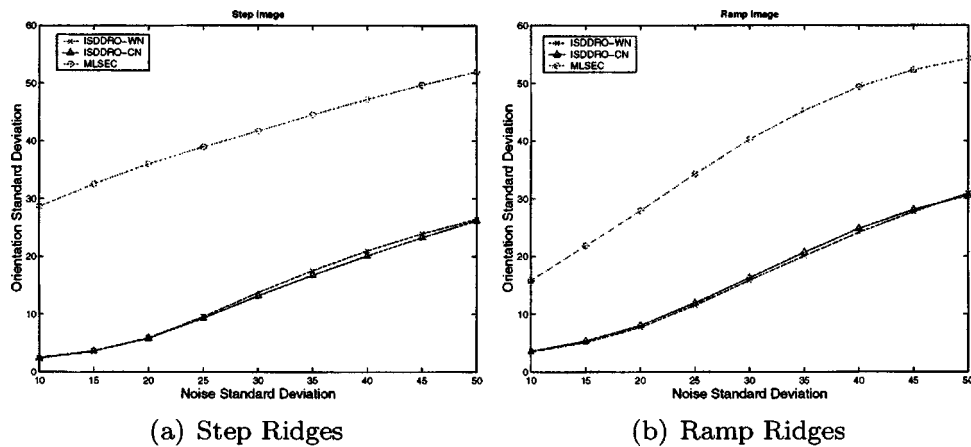


Fig. 12 Orientation standard deviation plotted against the noise standard deviation. The orientation set to 30° .

formance criterion ISDDRO-CN performs better under very noisy conditions compared to the other two operators for both step and ramp ridges.

6.3.4 Noise standard deviation versus orientation standard deviation

Figures 12(a) and 12(b) show the orientation standard deviation plotted against the noise standard deviation for step and ramp ridges, respectively. For these plots, we held the true orientation at 30° . For step ridges, ISDDRO-CN produces an orientation standard deviation curve that tracks the result produced by ISDDRO-WN until σ_η reaches 25 and after that it performs slightly better than ISDDRO-WN. For ramp ridges, ISDDRO-WN performs slightly better than ISDDRO-CN until $\sigma_\eta = 45$ and after that roles get reversed. MLSEC performs poorly with both step and ramp ridges. Again, under this criterion ISDDRO-CN performs better than the other two operators under high noise conditions.

7 Summary and Future Work

In this paper, we discussed a unified theory for and performance evaluation of the ridge orientation estimation through the minimization of the integral of the second directional derivative of the gray-level intensity function. Performance evaluation of the ridge orientation estimation is carried out as a function of the noise perturbation on the input image, in terms of the *mean orientation bias* and *orientation standard deviation* given the *true orientation* and the same two measures given the *noise standard deviation*. We discussed two forms of our new ridge detector one using the noise covariance matrix estimation procedure (ISDDRO-CN) and the second using the white noise assumption (ISDDRO-WN). We showed that ISDDRO-CN performs better than the ISDDRO-WN in the presence of strong correlated noise, where as when the noise levels are moderate it performs as well as ISDDRO-WN. ISDDRO-CN has superior noise sensitivity characteristics. We also compared both forms of our algorithm with the algorithm, MLSEC designed by López²² and found that our algorithm supersedes MLSEC in terms of noise sensitivity and the ridge orientation estimate bias and standard deviation. We performed this comparative evaluation using syn-

thetically generated images containing *step* and *ramp* images contaminated by colored noise with a given variance and correlation matrix. ISDDRO-CN algorithm uses the noise covariance matrix estimated by using the algorithm described in Refs. 41 and 42. We have used DOP bases—though any other functional form could have been used—mainly for its simplicity and mathematical tractability in the Bayesian statistical framework for noise covariance estimation described in Refs. 41 and 42.

In future work, we would like to compare our algorithms against the MLSEC-ST (MLSEC with Structure Tensor) algorithm by López²² in which the authors state that MLSEC-ST is an improvement over the MLSEC algorithm. The algorithms presented in this paper can also be extended to 3D, since the DOP bases can be extended to 3D in a similar fashion to extending 2D from 1D. However, extending the *noise covariance estimation* algorithm used in ISDDRO-CN may involve extensive rework of the theory and when implemented in software may involve significant computational complexity. The algorithms described in this paper were mainly designed for optimal ridge orientation estimation. We have not focused on the ridge pixel labeling. For this reason, all the experiments were performed on synthetically generated images with differing levels of noise with known ridge feature orientation. However, as part of the future work we are planning to extend the algorithms to use the estimated orientations in the ridge pixel labeling. We will, then, perform experiments on the real world images and report the results.

Acknowledgment

We thank Dr. López (Ref. 22) for providing the MLSEC code.

References

1. T. K. Peuker and E. G. Johnston, "Detection of surface-specific points by local parallel processing of discrete terrain elevation data," Technical Report 206, Computer Science Center, University of Maryland, College Park (1972).
2. T. K. Peuker and D. H. Douglas, "Detection of surface-specific points by local parallel processing of discrete terrain elevation data," *Comput. Graph. Image Process.* **4**, 375–387 (1975).
3. E. G. Johnston and A. Rosenfeld, "Digital detection of pits, peaks, ridges, and ravines," *IEEE Trans. Syst. Man Cybern.* **5**, 472–480 (1975).

4. K. Paton, "Picture description using Legendre polynomials," *Comput. Vis. Graph. Image Process.* **4**, 40–54 (1975).
5. G. C. Grender, "TOPO: A Fortran Program for terrain analysis," *Comput. Geosci.* **2**, 195–209 (1976).
6. J. Toriwaki and T. Fukumura, "Extraction of structural information from grey pictures," *Comput. Graph. Image Process.* **7**, 30–51 (1978).
7. S. Hsu, J. L. Mundy, and P. R. Beaudet, "Web representation of image data," in *Proceedings of the Fourth International Conference on Pattern Recognition*, pp. 675–680 (1978).
8. H. C. Lee and K. S. Fu, "The GLGS image representation and its application to preliminary segmentation," in *Proceedings of the 1981 Conference on Pattern Recognition and Image Processing*, New York, pp. 256–261 (1981).
9. R. M. Haralick, "Ridges and valleys on digital images," *Comput. Vis. Graph. Image Process.* **22**, 28–38 (1983).
10. R. M. Haralick, "Cubic facet model edge detector and ridge-valley detector: Implementation details," in *Pattern Recognition in Practice II*, edited by E. S. Gelsema and L. N. Kanal, pp. 81–90, Elsevier Science (North-Holland), Netherlands (1986).
11. S. Chinveeraphan, R. Takamatsu, and M. Sato, "Understanding of ridge-valley lines on image-intensity surfaces in scale-space," in *6th International Conference on Computer Analysis of Images and Patterns, CAIP'95*, pp. 661–667 (1995).
12. T. Lindeberg, "Junction detection with automatic selection of detection scales and localization scales," in *International Conference on Image Processing*, Vol. 1, pp. 924–928 (1994).
13. T. Lindeberg, "Edge detection and ridge detection with automatic scale selection," in *IEEE Computer Society Conference on Computer Vision and Pattern Recognition*, pp. 465–470 (1996).
14. P. Sukanya, R. Takamatsu, and M. Sato, "The surface-shape operator based shading-tolerant method for multiscale image analysis," in *International Conference on Image Processing*, Vol. 1, pp. 221–225 (1998).
15. O. Monga, S. Benayoun, and O. D. Faugeras, "From partial derivatives of 3D density images to ridge lines," in *IEEE Computer Society Conference on Computer Vision and Pattern Recognition*, pp. 354–359 (1992).
16. J. B. Subirana-Vilanova and K. K. Sung, "Ridge-detection for the perceptual organization without edges," in *4th International Conference on Computer Vision*, pp. 57–64 (1993).
17. J. Hou and R. H. Bamberger, "Orientation selective operators for ridge, valley, edge, and line detection in imagery," in *IEEE International Conference on Acoustics, Speech and Signal Processing, IC-ASSP'94*, pp. V/25–V/28 (1994).
18. P. Sukanya, R. Takamatsu, and M. Sato, "A new operator for image structure analysis," in *International Conference on Image Processing*, Vol. 3, pp. 615–618 (1996).
19. P. Sukanya, H. Tanuma, R. Takamatsu, and M. Sato, "A new operator for describing topographical image structure," in *13th International Conference on Pattern Recognition*, pp. 50–54 (1996).
20. P. G. Ducksbury, M. J. Varga, Z. Y. Xie, and J. M. Brady, "Image content descriptors: The detection stage," in *IEEE Colloquium on Intelligent Image Databases*, pp. 5/1–5/6 (1996).
21. P. G. Ducksbury and M. J. Varga, "Region based image content descriptors and representation," in *6th International Conference on Image Processing and Its Applications*, Vol. 2, pp. 561–565 (1997).
22. A. M. López, F. Lumberras, J. Serrat, and J. J. Villanueva, "Evaluation of methods for ridge and valley detection," *IEEE Trans. Pattern Anal. Mach. Intell.* **21**, 327–335 (1999).
23. A. G. Bors, E. R. Hancock, and R. C. Wilson, "Terrain feature identification by modeling radar image statistics," in *International Conference on Image Processing*, Vol. 1, pp. 721–724 (2000).
24. A. G. Bors, E. R. Hancock, and R. C. Wilson, "3-D terrain from synthetic aperture radar," in *IEEE Workshop on Computer Vision Beyond the Visible Spectrum: Methods and Applications*, Vol. 1, pp. 63–72 (2000).
25. L. Tao, S. Oe, H. Murai, and K. Inouchi, "Mountain areas extraction by introduction of wavelet transform and its applications to ridge lines detection," *Journal of the Institute of Image Electronics Engineers of Japan* **30**, 293–297 (2001).
26. A. G. Bors, E. R. Hancock, and R. C. Wilson, "A Bayesian framework for radar shape-from-shading," in *IEEE Conference on Computer Vision and Pattern Recognition*, Vol. 1, pp. 262–268 (2000).
27. J. Stoeckel, F. M. Vos, P. H. Vos, and A. M. Vossepoel, "An evaluation of ridge extraction methods for portal imaging," in *15th International Conference on Pattern Recognition*, Vol. 3, pp. 429–432 (2000).
28. G. Subsol, J. Ph. Thirion, and N. Ayache, "Nonrigid registration for building 3D anatomical atlases," in *12th IAPR International Conference on Pattern Recognition, Conference A: Computer Vision and Image Processing*, Vol. 1, pp. 576–578 (1994).
29. J. B. A. Maintz, P. A. van den Elsen, and M. A. Viergever, "Evaluation of ridge seeking operators for multimodality medical image matching," *IEEE Trans. Pattern Anal. Mach. Intell.* **18**, 353–365 (1996).
30. D. Lloret, A. M. López, and J. Serrat, "Creaseness-based CT and MR registration: Comparison with the mutual information method," *J. Electron. Imaging* **8**, 255–262 (1999).
31. Y. Hoshino, "Automated fingerprint identification system (AFIS)," *NEC Technical Journal* **45**(4), 100–104 (1992).
32. D. Maio and D. Maltoni, "Direct gray-scale minutiae detection in fingerprints," *IEEE Trans. Pattern Anal. Mach. Intell.* **19**, 27–40 (1997).
33. I. G. Bae, B. H. Cho, J. S. Kim, J. H. Bae, and K. Y. Yoo, "Online fingerprint verification system using direct minutiae extraction," in *ISCA 13th International Conference on Computer Applications in Industry and Engineering*, pp. 120–123 (2000).
34. J. H. Chang and K. C. Fan, "Fingerprint ridge allocation in direct gray-scale domain," *Pattern Recogn.* **34**, 1907–1925 (2001).
35. A. Almansa and T. Lindeberg, "Fingerprint enhancement by shape adaptation of scale-space operators with automatic scale selection," *IEEE Trans. Image Process.* **9**, 2027–2042 (2000).
36. E. Salari, "A method for medial line transformation," in *IEEE International Conference on Systems, Man and Cybernetics*, Vol. 1, pp. 815–817 (1986).
37. T. V. Nguyen and J. Sklansky, "Computing the skeleton of coronary arteries in cineangiograms," *Journal of Computers and Biomedical Research* **19**(5), 428–444 (1986).
38. Y. Kawata, N. Niki, H. Ohmatsu, R. Kakinuma, K. Eguchi, M. Kaneko, and N. Moriyama, "Classification of pulmonary nodules in thin-section CT images based on shape characterization," in *IEEE Computer Society International Conference on Image Processing*, Vol. 3, pp. 528–530 (1997).
39. A. M. López, W. Niessen, J. Serrat, K. Nicolay, B. Ter Haar Romeny, J. Villanueva, and M. Viergever, "New improvements in the multiscale analysis of trabecular bone patterns," in *Pattern Recognition and Applications (Frontiers in Artificial Intelligence and Applications)*, Vol. 56, pp. 251–260 (2000).
40. R. M. Haralick and L. G. Shapiro, *Computer and Robot Vision*, Vol. 1, Addison-Wesley, Reading (1992).
41. D. Nadadur, "Noise covariance estimation in low-level computer vision," Ph.D. thesis, Box 352500, Department of Electrical Engineering, University of Washington, Seattle, Washington (2001).
42. D. Nadadur, R. M. Haralick, and D. E. Gustafson, "A Bayesian framework for noise covariance estimation using the facet model," *IEEE Transactions on Image Processing* (submitted).
43. G. E. Forsythe, "Generation and use of orthogonal polynomials for data-fitting with a digital computer," *Journal of the Society for Industrial Applied Mathematics* **5**, 74–88 (1957).
44. O. A. Zuniga and R. M. Haralick, "Integrated directional derivative gradient operator," *IEEE Trans. Syst. Man Cybern.* **SMC-17**, 508–517 (1987).
45. W. H. Press, S. A. Teukolsky, W. T. Vetterling, and B. P. Flannery, *Numerical Recipes in C: The Art of Scientific Computing*, 2nd ed., Cambridge University Press (1992).
46. D. Nadadur and R. M. Haralick, "Recursive binary dilation and erosion using digital line structuring elements in arbitrary orientations," *IEEE Trans. Image Process.* **9**(5), 749–759 (2000).



Desikachari Nadadur received his Bachelor of Technology (BTech) degree in Electronics and Communications Engineering from Sri Venkateswara University, Tirupati, Andhra Pradesh, India, in 1990 and his Master of Science (MS) degree in Electrical Engineering from Gonzaga University, Spokane, Washington, U.S.A., in 1993. In November 2001, he received his Doctor of Philosophy (PhD) degree in Electrical Engineering with a specialization in Image

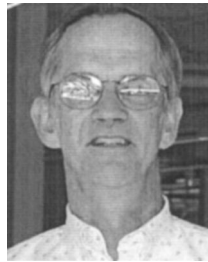
Processing and Computer Vision from University of Washington, Seattle, Washington, U.S.A., under the supervision of Professor Robert M. Haralick. His dissertation was titled, "Noise covariance estimation in low-level computer vision." Since 1999, he has been a Senior Scientist in the Advanced Imaging Applications group of the Developing Competency Department at Siemens Medical Solutions, Inc., Ultrasound Division, Issaquah, Washington, U.S.A. He was a Teaching Assistant in the department of Electrical Engineering, Gonzaga University, Spokane, Washington, U.S.A., from 1991 to 1993. He was a Predoctoral Research Associate II, at the Intelligent Systems Laboratory (ISL), University of Washington, Seattle, from 1993 to 1997. He worked as a Software Engineer in the Advanced Technologies Group at Electronics for Imaging, Inc., Foster City, California, U.S.A., from 1997 to 1999. Dr. Nadadur has co-authored several publications in the field of image processing, mathematical morphology and computer vision and holds several patents. His current re-

search interests include: application of deformable, finite element models, PDE and level set methods to medical image segmentation, Bayesian and other statistical methods in image analysis, performance characterization of vision algorithms.



Robert Martin Haralick is a Distinguished Professor in the Department of Computer Science at the Graduate Center, City University of New York. He was the Boeing Clairmont Egtvedt Professor in the Department of Electrical Engineering, University of Washington, Seattle. He is responsible for developing the gray scale co-occurrence texture analysis technique and the facet model technique for the image processing. He has worked on robust

methods for photogrammetry and developed fast algorithms for solving the consistent labeling problem in high-level computer vision. He has developed shape analysis and extraction techniques using mathematical morphology, the morphological sampling theorem, and fast recursive morphology algorithms. Together with Professor I. Phillips, he has developed a comprehensive ground-truthed set of some 1600 document image pages (most in English) and some 200 pages in Japanese in the area of document image understanding. He has also developed algorithms for document skew angle estimation, zone delineation, and word and text line bounding box delineation. His most recent research is in the area of computer vision performance characterization and covariance propagation. He has published more than 490 papers. Dr. Haralick is a Fellow of IEEE for his contributions in computer vision and image processing and a Fellow of the International Association for Pattern Recognition (IAPR) for his contributions in pattern recognition, image processing, and for services to IAPR. He was also the President of the IAPR.



David Earl Gustafson received his Bachelor of Arts degree in Physics from Hamline University and his Doctor of Philosophy degree in Physics from University of Virginia. He was a Nuclear Physics Postdoctoral Fellow, Florida State University and a Postdoctoral Research Fellow at Mayo Clinic. He is at present a Senior Director at Siemens Medical Solutions USA Inc., Ultrasound Division, Issaquah, Washington. Dr. Gustafson has extensive experience

including medical imaging research and development in both university academic and industrial settings. Five years experience in academia, including teaching in radiology residency and technologist programs, and 24 years in the medical imaging industry. Industry positions, which included group to department managerial roles for 20 years, have focused on conducting and directing product research and development, with strong focus on extensive strategic advanced development carrying product features from inception to product release. His experience has also included manufacturing, marketing and business management responsibility and management of multisite development teams, widely diversified geographically, including extensive R & D staff consisting of engineers and scientists, most with advanced degrees, and product development marketing personnel. Development projects have covered most modern medical imaging methods. Broad imaging and image processing product development experience includes: computed tomography, digital x-ray fluoroscopy, radiography and angiography products, mobile x-ray systems, image-intensified special procedures radiology and cardiology systems, mammography, ultrasound, PACS and connectivity, CAD, and nuclear medicine products.